

Ising Supercriticality and Universal Magnetocalorics in Spiral Antiferromagnet Nd_3BWO_9

Xinyang Liu,^{1,2,*} Enze Lv,^{3,*} Xueling Cui,¹ Han Ge,⁴ Fangyuan Song,⁵ Liusuo Wu,⁴ Zhaoming Tian,⁵ Peijie Sun,² Gang Su,³ Kan Zhao,^{1,†} Junsen Xiang,^{2,‡} and Wei Li^{3,6,§}

¹*School of Physics, Beihang University, Beijing 100191, China*

²*Beijing National Laboratory for Condensed Matter Physics,*

Institute of Physics, Chinese Academy of Sciences, Beijing 100190, China

³*Institute of Theoretical Physics, Chinese Academy of Sciences, Beijing 100190, China*

⁴*Department of Physics, Southern University of Science and Technology, Shenzhen, China*

⁵*School of Physics and Wuhan National High Magnetic Field Center,*

Huazhong University of Science and Technology, Wuhan 430074, China

⁶*Peng Huanwu Collaborative Center for Research and Education, Beihang University, Beijing 100191, China*

(Dated: January 13, 2026)

The celebrated analogy between the pressure-temperature phase diagram of a liquid-gas system and the field-temperature phase diagram of an Ising ferromagnet has long been a cornerstone for understanding universality in critical phenomena. Here we extend this analogy to a highly frustrated antiferromagnet, the kagome-layered spiral Ising compound Nd_3BWO_9 . In its field-temperature phase diagram, we identify a critical endpoint (CEP) and an associated Ising supercritical regime (ISR). The CEP of the metamagnetic transition is located at $\mu_0 H_c \simeq 1.04$ T and $T_c \simeq 0.3$ K. Above this point, the ISR emerges with supercritical crossover lines that adhere to a universal scaling law, as evidenced by the specific heat and magnetic susceptibility measurements. Remarkably, we observe a universally divergent Grüneisen ratio near the emergent CEP, $\Gamma_H \propto 1/t^{\beta+\gamma-1}$, with $\beta + \gamma \simeq 1.563$ the critical exponents of the 3D Ising universality class and $t \equiv (T - T_c)/T_c$ the reduced temperature. Our adiabatic demagnetization measurements on Nd_3BWO_9 reveal a lowest temperature of 195 mK achieved from 2 K and 4 T. Our work opens new avenues for studying supercritical physics and efficient cooling in layered-kagome, rare-earth RE_3BWO_9 family and, more broadly, in Ising-anisotropic magnets like spin ices.

Introduction.— Frustrated spin systems offer an ideal platform for uncovering exotic magnetic states and transitions [1–6]. Among them, rare-earth magnets are particularly compelling, where the interplay of geometric and interaction frustration can give rise to a rich landscape of exotic spin states [7–13]. Recently, a new family of rare-earth layered-kagome compounds, RE_3BWO_9 ($\text{RE} = \text{Pr-Sm, Gd-Ho}$) is discovered [14, 15]. In particular, the compound Nd_3BWO_9 hosts magnetic Nd^{3+} ions that form spin-orbit Kramers doublets, constituting an effective $S = 1/2$ frustrated antiferromagnet [16–19]. Initially, its kagome-layered structure was thought to potentially host a quantum spin liquid phase [15, 16], sparking significant research interests.

Recent neutron scattering studies have established an antiferromagnetic (AF) order in Nd_3BWO_9 below 0.3 K [16], ruling out a quantum-spin-liquid ground state. Subsequent measurements revealed a complex spin order due to the triple braids of spiral Ising axes. The AF, 1/3-plateau, and partially polarized states are separated by two first-order metamagnetic transitions due to the strong magnetic anisotropy [17]. A magnetization jump occurs at the metamagnetic transition from the 1/3-plateau to the partially polarized phase [Fig. 1(b)] [17, 18]. This jump vanishes above a critical temperature, as shown schematically in Figs. 1(d-f); however, round peaks in specific heat (C_p) persist at significantly higher temperatures, forming two “ridges” emanating from the critical endpoint (CEP) [18], as shown in Figs. 2(a,b). A rich field-temperature phase diagram has been mapped out by magnetic and thermodynamic measurements [16, 18], complemented by low-energy dynamical probes (μSR , NMR) of

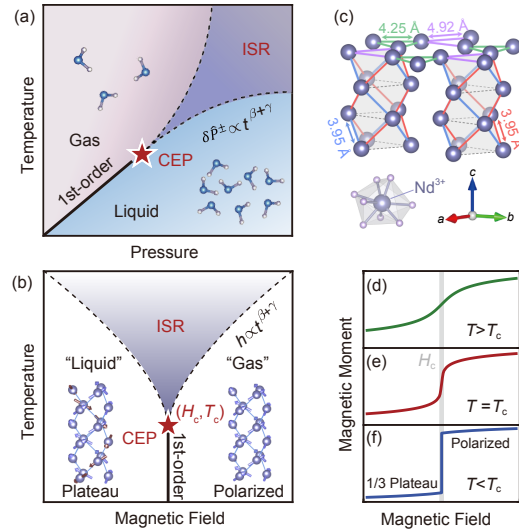


FIG. 1. Schematic phase diagrams of (a) water and (b) Nd_3BWO_9 , where the solid line represents a first-order transition and red star denotes the CEP. For Nd_3BWO_9 , the metamagnetic transition line separates 1/3-plateau (“liquid”) and partially polarized (“gas”) phases, and the dashed lines enclose the Ising supercritical regime (ISR). The universal supercritical crossover scaling is $\delta \hat{P}^\pm \propto t^{\beta+\gamma}$ for water [20], and $h \propto t^{\beta+\gamma}$ for Nd_3BWO_9 . $\delta \hat{P}^\pm$ is the reduced pressure, $h \equiv (H - H_c)/H_c$ is the reduced field, and $t \equiv (T - T_c)/T_c$ is the reduced temperature. β and γ are critical exponents of 3D Ising universality class. (c) Coupled spin tubes of Nd^{3+} and distorted NdO_8 octahedron. (d-f) Schematic plots of magnetization curves above, at, and below T_c .

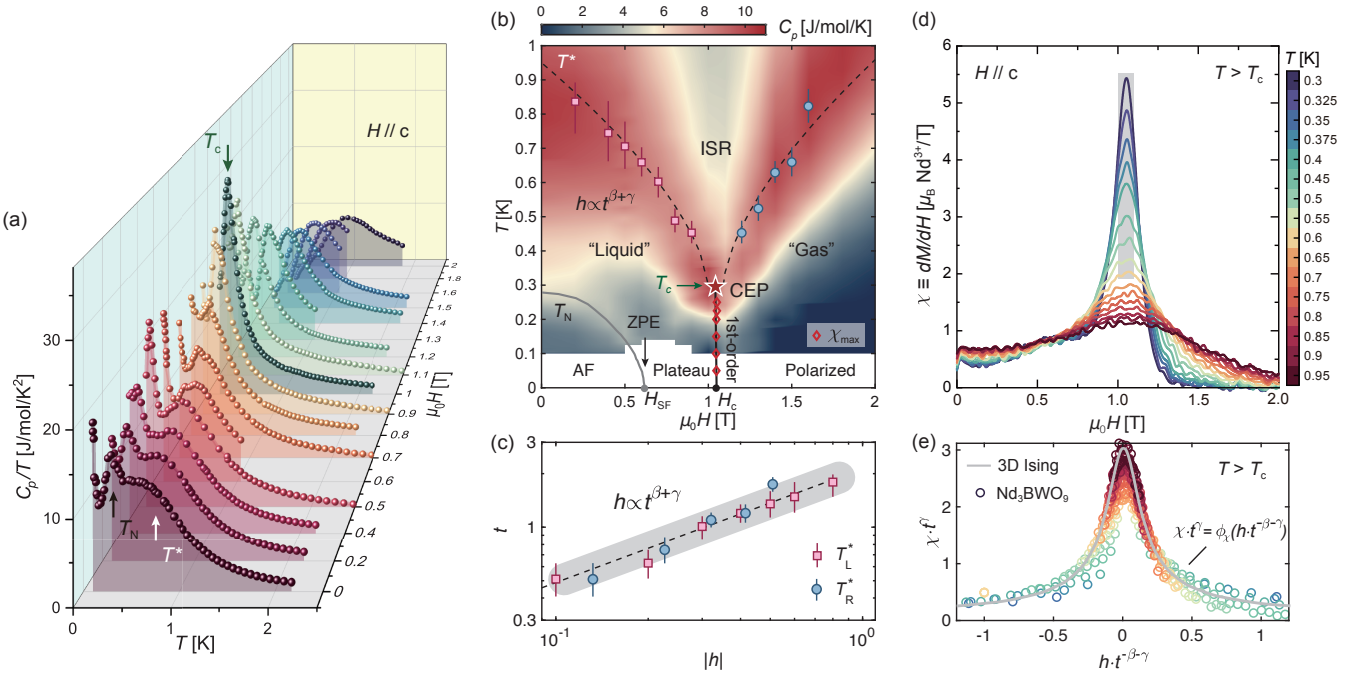


FIG. 2. (a) Low-temperature specific heat (C_p/T) of Nd_3BWO_9 under c -axis magnetic fields from 0 T to 2 T. (b) Color map of C_p , where the maxima for $H < H_c$ (red squares) and $H > H_c$ (blue circles) denote the supercritical crossovers (dashed black lines). The uncertainty (error bar) is estimated by the temperature step size in the specific heat measurements. The star marks the CEP at $\mu_0 H_c = 1.04(4)$ T and $T_c = 0.30(2)$ K. The uncertainties reflect the variation across different measurements, including the specific heat, magnetization, and magnetocalorics. The solid black line below the CEP represents the first-order metamagnetic transition line. The red diamonds mark the peak positions of $\chi \equiv dM/dH$ below T_c , which are used to identify the first-order line (see Supplementary Fig. S1). Above the CEP, there exists an ISR which separates the “liquid” and “gas” states. The gray dot indicates the spin-flip field $\mu_0 H_{SF} \simeq 0.65$ T, and the solid gray line is the AF phase boundary. (c) Supercritical crossover scaling law $h \propto t^{\beta+\gamma}$, with β and γ the critical exponents of 3D Ising universality class. The reduced temperature $t = |T_{L,R}^* - T_c|/T_c$, with T_L^* and T_R^* the peak positions in the left and right branches of C_p in panel (b), respectively. (d) Magnetic susceptibility χ as a function of magnetic field at various temperatures above T_c . (e) Data collapse of the measured χ results in the supercritical regime, whose profile is in excellent agreement with the universal scaling function $\phi_\chi(x)$ theoretically obtained from calculating the 3D Ising model (see Appendix). Data in the gray region are omitted from the collapse due to limited resolution in this highly field-sensitive regime, where the χ divergence is suppressed by the finite field step.

spin fluctuations [19]. These measurements collectively establish Nd_3BWO_9 as a compelling platform for investigating field-induced spin state transitions and critical phenomena.

In this work, we perform comprehensive low-temperature thermodynamic and magnetocaloric measurements. In the phase diagram of Nd_3BWO_9 , we identify a field-induced first-order metamagnetic line that terminates at the CEP with $\mu_0 H_c = 1.04(4)$ T and $T_c = 0.30(2)$ K. Above this point, there exhibits an Ising supercritical regime (ISR) in this 3D spiral Ising compound [see Fig. 1(c)]. This magnetic ISR follows the same universal scalings as those of the liquid-gas supercritical regime [see Figs. 1(a,b)], accounting for the specific heat anomalies and the magnetization behaviors observed in experiments. In particular, the supercritical crossovers are characterized by a universal scaling $h \propto t^{\beta+\gamma}$ (t and h being reduced parameters) with $\beta + \gamma \simeq 1.563$ of the 3D Ising universality class [see Fig. 1(b)] [21]. This is further confirmed by obtaining the 3D Ising supercritical scaling function $\phi_\chi(x)$ through measuring and collapsing the magnetic susceptibility data. Our findings thus establish an antiferromagnetic realiza-

tion of liquid-gas Ising supercriticality.

Remarkably, the high field-sensitivity near the CEP gives rise to a pronounced supercritical magnetocaloric effect (MCE), characterized by the universally diverging Grüneisen ratio, $\Gamma_H \equiv 1/T(\partial T/\partial H)_S \propto 1/t^{\beta+\gamma-1}$. Through adiabatic demagnetization measurements, we achieve a lowest cooling temperature of 195 mK with Nd_3BWO_9 , enabled by the supercritical MCE near H_c and also the cooling near the lower spin-flip field ($\mu_0 H_{SF} \simeq 0.65$ T). The latter can be ascribed to the proximate zero-point entropy of proliferated topological defects. Our results establish Nd_3BWO_9 as an efficient sub-Kelvin coolant, further underpinned by exceptionally high spin density in this boratotungstate. Moreover, the universality of supercritical MCE suggests its broad applicability in other magnetic systems with strong Ising anisotropy and local constraints like spin-ice magnets [22–31].

Universal thermal data with supercritical scaling.— We synthesize high-quality Nd_3BWO_9 single crystals (see Appendix) and measured the specific heat C_p/T under c -axis magnetic fields down to 100 mK [see Fig. 2(a)]. Under

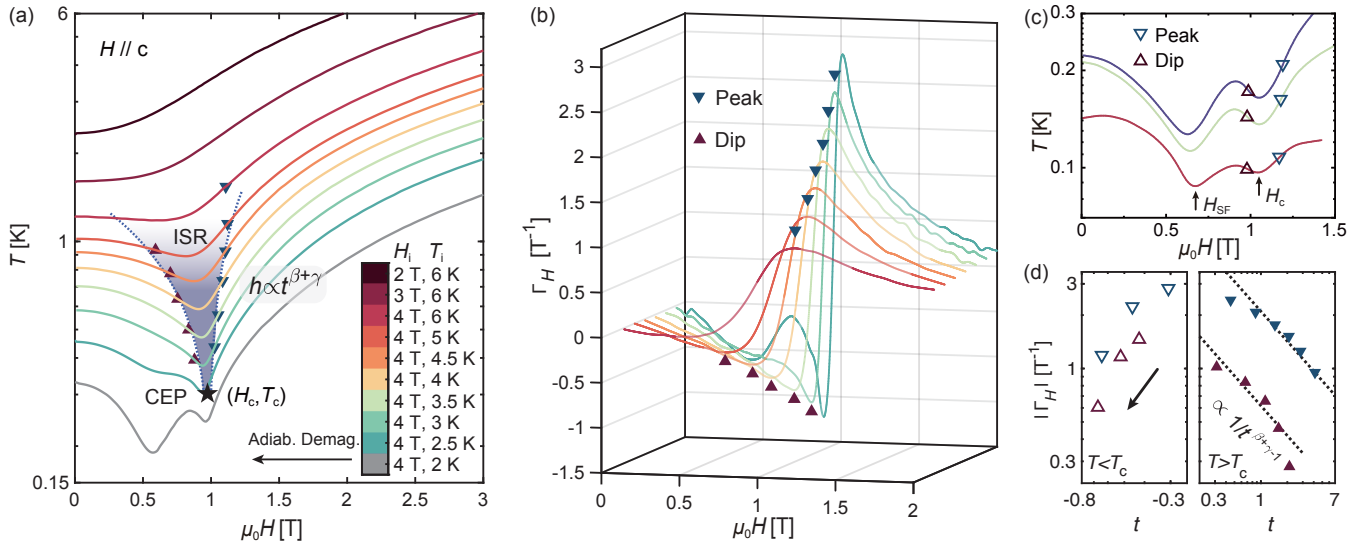


FIG. 3. (a) The isentropes obtained via adiabatic demagnetization measurements, with legends specifying the initial conditions (H_i, T_i) . The supercritical crossover line (blue dotted line) $h \propto t^{\beta+\gamma}$ are determined from the peak/dip positions of the magnetic Grüneisen ratio $\Gamma_H \equiv \frac{1}{T} \left(\frac{\partial T}{\partial H} \right)_S$ shown in (b), which are derived from the isentropic lines. Blue and red triangles mark the peaks and dips of Γ_H , respectively. (c) Isentropic lines of Nd_3BWO_9 below $T_c \simeq 0.3$ K. Hollow triangles denote the peak/dip positions of corresponding Γ_H . (d) Temperature dependence of the peak/dip values of Γ_H . The black dashed line indicates the supercritical magnetocaloric scaling $\Gamma_H \propto 1/t^{\beta+\gamma-1}$ for $t > 0$ (i.e., $T > T_c$). Very close to T_c , we find deviation of Γ_H from this scaling, which owes to the measurement accuracy. On the subcritical side ($t < 0$), these extrema decrease rapidly.

zero field, the specific heat exhibits a sharp peak at about $T_N \simeq 0.29$ K, signaling the onset of AF order. With increasing field, this peak shifts to lower temperatures and vanishes at around $\mu_0 H_{SF} \simeq 0.65$ T. Notably, a broad hump observed at $T^* \simeq 1$ K (under zero field), which marks the buildup of short-range spin correlations, shifts downward with increasing field. The hump position reaches a minimum temperature of about 0.3 K near H_c before turning upward at higher fields [see the contour plot of C_p in Fig. 2(b)].

We denote the hump locations as $T_{L,R}^*$, which delineate the finite-temperature ISR and follow a universal scaling $h \propto t^{\beta+\gamma}$ following 3D Ising universality class [see Fig. 2(c)]. The order parameter for the first-order transition between the 1/3-plateau and partially polarized phases is the total magnetization. This is analogous to the density difference across the liquid-gas phase boundary. Therefore, with the CEP located at $T_c \simeq 0.3$ K and $\mu_0 H_c \simeq 1.04$ T, and by employing the 3D Ising critical exponents β and γ , we can accurately reproduce the scaling behaviors of these $T_{L,R}^*$ boundaries. Such scaling behavior originates from the universal form of specific heat in the supercritical regime, i.e., $C(H, T) = t^{-\alpha} \phi_C(x)$, where $\phi_C(x)$ with $x \equiv h \cdot t^{-\beta-\gamma}$ is the scaling function derived from singular part of the free energy (see Appendix). We emphasize that while the emergent CEP is a single point in the phase diagram and thus difficult to pinpoint, the associated ISR — which extends over a broad region and is characterized by robust supercritical scaling — is considerably more accessible in experiments.

In addition, we conducted ultralow-temperature magnetization measurements to determine the metamagnetic transi-

tion at $\mu_0 H_c \simeq 1.04$ T from the magnetization jump (see Supplementary Fig. S1). The magnetic susceptibility can be obtained from the magnetization measurements, via differentiation $\chi \equiv dM/dH$. We show the supercritical data in Fig. 2(d), where the series of peaks near H_c indicates the high field-sensitivity; Below T_c , the χ peak values saturate, as the numerical differentiation involves a finite step length in computing dM/dH from experimental data. Such a behavior is consistent with a CEP at finite T_c rather than a quantum critical scenario. According to the scaling analysis, magnetic susceptibility follows a universal scaling form $\chi(H, T) = t^{-\gamma} \phi_\chi(h \cdot t^{-\beta-\gamma})$ above the CEP (see Appendix). By rescaling $x \equiv h \cdot t^{-\beta-\gamma}$ and $y \equiv \chi \cdot t^\gamma$ with the critical exponents $\beta \simeq 0.326$ and $\gamma \simeq 1.237$, we collapse the magnetic susceptibility data onto a single curve [see Fig. 2(e)]. Notably, we further find the collapsed data agree excellently with the calculated scaling function $\phi_\chi(x)$ for the 3D Ising universality class (see details in Appendix).

Supercritical magnetocaloric effect.— The adiabatic demagnetization measurements of Nd_3BWO_9 starting from different initial conditions yield its isentropic lines. As shown in Fig. 3(a), there appear isentrope dips within the ISR, due to the strong spin fluctuations present above the CEP. The corresponding magnetic Grüneisen ratio Γ_H , derived from the isentropic lines, displays a peak-dip structure [see Fig. 3(b)]. As the temperature approaches T_c , the peak and dip positions asymptotically approach H_c . Moreover, in Fig. 3(d), we find the peak/dip values obey a supercritical magnetocaloric scaling law $\Gamma_H \propto 1/t^{\beta+\gamma-1}$, which can be derived from the universal form of free energy (see Appendix). Below T_c , the isen-

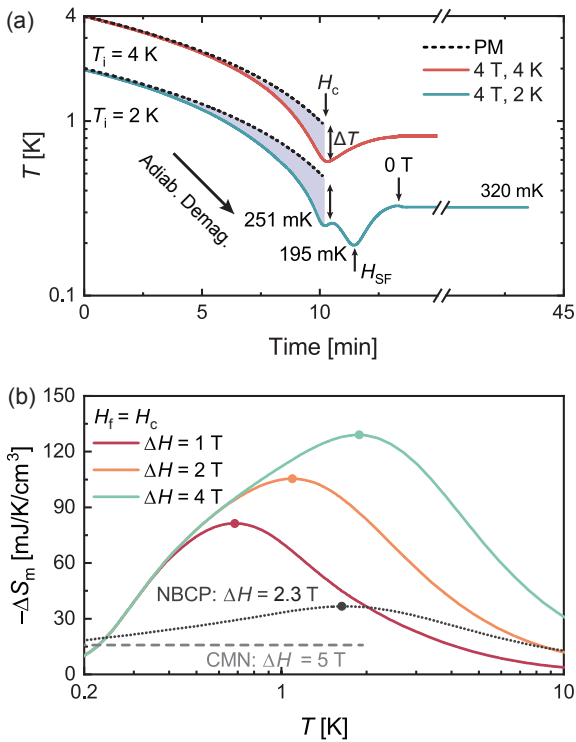


FIG. 4. (a) ADR process under fields along the c -axis. The green and red solid lines are for different initial temperatures $T_i = 4$ K and 2 K, respectively, both at the initial field $\mu_0 H_i = 4$ T. The black dashed lines represent the cooling curves of ideal paramagnetic (PM) salt. The purple shaded areas highlight the enhanced cooling effect in Nd_3BWO_9 compared to the PM salt, characterized by ΔT , which equals 414 mK and 249 mK for curves from $T_i = 4$ K and 2 K, respectively. (b) Volumetric magnetic entropy change ($-\Delta S_m$) for Nd_3BWO_9 under different field changes (final field at $\mu_0 H_f = \mu_0 H_c \simeq 1$ T). The dots mark the maximum of each curve. The black dotted line shows the spin supersolid compound $\text{Na}_2\text{BaCo}(\text{PO}_4)_2$ (NBCP) under a field change from 4 T to its critical field 1.7 T [32]; and the gray dashed line shows a prototypical PM coolant $\text{Ce}_2\text{Mg}_3(\text{NO}_3)_{12} \cdot 24\text{H}_2\text{O}$ (CMN) under a field change of 5 T.

trope dips near H_c grow progressively shallower at lower temperatures, as evidenced in Fig. 3(c). This reflects the weakened cooling effect due to the minimum entropic effects of the metamagnetic transitions.

Proximate zero-point entropy and self-cascading cooling.— Figure 4(a) illustrates two representative adiabatic demagnetization refrigeration (ADR) measurements starting from $(\mu_0 H_i, T_i) = (4 \text{ T}, 4 \text{ K})$ and $(4 \text{ T}, 2 \text{ K})$, respectively. Upon decreasing the fields to H_c , Nd_3BWO_9 reaches a lower temperature than the PM salt, characterized by the substantial temperature difference ΔT . Unlike the cooling curve starting from $T_i = 4$ K, which reaches its lowest temperature of 586 mK at H_c , the process beginning at $T_i = 2$ K attains its lowest temperature of 195 mK at the spin-flip field $\mu_0 H_{\text{SF}} \simeq 0.65$ T [see also Fig. 3(a,c)]. Matter of fact, the zero-field entropy curves obtained from specific heat mea-

surements exhibit a shoulder at $S = S_0 \simeq 0.481 \text{ R}$ (see Fig. 7), which can be attributed to a proximate zero-point entropy (ZPE) from topological domain-wall proliferation (see explanation below). Moreover, the low- T entropy is further enhanced at H_{SF} , accounting for the shift of the minimum cooling temperature to this spin-flip field.

To interpret these features, we perform model calculations involving the spiral Ising tube [17] (see Appendix for details). We uncover a first-order metamagnetic transition at H_{SF} carrying a macroscopic ground-state degeneracy, with a calculated ZPE of $S_0 \simeq 0.481 \text{ R}$ per unit cell. This extensive degeneracy can be ascribed to the presence of magnetic domain walls — topological defects that correspond to global spin flips throughout the spiral Ising tube. Therefore, for the cooling curve from initial temperature of $T_i = 2$ K, there exhibits a self-cascading process between two cooling stages: one driven by supercritical fluctuations near H_c and the other by ZPE release at H_{SF} . It is such self-cascading mechanism in Nd_3BWO_9 that achieves the lowest temperature of 195 mK.

Large entropy change driven by small field variation.— A key figure of merit for a magnetic refrigerant is its volumetric magnetic entropy change $-\Delta S_m \equiv S_m(H_f, T) - S_m(H_i, T)$, which largely determines practical cooling performance. For Nd_3BWO_9 , we calculated $-\Delta S_m$ for each field change using the entropy data integrated from the measured specific heat C_m (see Appendix). For a modest 1 T field change (and stopping at $H_f = H_c$), we find a large entropy change of $-\Delta S_m \simeq 83 \text{ mJ} \cdot \text{K}^{-1} \cdot \text{cm}^{-3}$ in the sub-Kelvin regime [see Fig. 4(b)]. This is substantially higher than the value of 37 $\text{mJ} \cdot \text{K}^{-1} \cdot \text{cm}^{-3}$ for NBCP, which was measured under a field change from 4 T to 1.7 T near the supersolid QCP, reflecting the high field-sensitivity of supercritical MCE in Nd_3BWO_9 . This value also far exceeds that of spin-1/2 hydrated PM salts, attributed to the exceptionally high spin density ($N \simeq 16.9 \text{ nm}^{-3}$), an order of magnitude greater than that of the hydrate CMN ($N \simeq 1.65 \text{ nm}^{-3}$).

Furthermore, a comparison with FM coolants of comparable spin density, such as LiHoF_4 ($N \simeq 13.7 \text{ nm}^{-3}$), reveals that while the latter exhibits high field-sensitivity, its ordering temperature is significantly higher ($T_c \simeq 1.53$ K) [33–35]. This highlights a key distinction: in Nd_3BWO_9 , the CEP is an emergent phenomenon that is greatly suppressed by magnetic frustration, despite the high spin density. This underscores the unique balance in Nd_3BWO_9 and, more broadly, in frustrated Ising antiferromagnets. For instance, the spin-ice compound $\text{Dy}_2\text{Ti}_2\text{O}_7$ has a comparable spin density ($N \simeq 15.44 \text{ nm}^{-3}$) and similarly hosts a low- T_c CEP at 360 mK [23]. We anticipate that it should exhibit a similar supercritical MCE. Further detailed comparisons are provided in Supplementary Table I.

Discussion.— Above the CEP of liquid-gas transition, the liquid and gas states become indistinguishable. They form a strongly fluctuating supercritical fluid widely used in refrigeration, engines, and power generation [36–39]. Their unique properties and universal behaviors originate from scale invariance near the CEP, as highlighted by the supercritical crossover lines that follow the 3D Ising scal-

ing. The fundamental correspondence between liquid–gas and magnetic transitions has long been established through finite-temperature CEP (i.e., Curie point) and supercritical fluctuations in ferromagnets. This well-established analogy has, in turn, spurred growing interest in the search for supercritical phenomena within frustrated antiferromagnets [20, 28, 40–45]. Notably, in the Shastry–Sutherland compound $\text{SrCu}_2(\text{BO}_3)_2$, a finite-temperature CEP has been found in its pressure–temperature phase diagram [40]; however, its pressure-driven supercritical scaling behaviors and associated magnetic barocaloric effect [41] remain challenging to access in experiments.

Here we report the discovery of a field-driven supercritical regime in the spiral Ising antiferromagnet Nd_3BWO_9 , emerging above a CEP of metamagnetic first-order transition line, and observe high-performance sub-Kelvin refrigeration in this compound. A lowest temperature of 195 mK is achieved through self-cascading between two field-induced metamagnetic transitions: one at $\mu_0 H_c \simeq 1.04$ T associated with a low-temperature CEP and the other at $\mu_0 H_{\text{SF}} \simeq 0.65$ T with proximate ZPE. The MCE has evolved from its origins in ferromagnets [46] to modern systems with low transition temperatures [33, 35, 47, 48]. We pursue a different approach by exploiting highly frustrated antiferromagnets with a low-temperature CEP and emergent ISR. The compound Nd_3BWO_9 intrinsically combines high spin density with low operating temperatures, exhibiting high-field sensitivity in temperature variation via supercritical MCE.

Our investigation offers valuable insights into other members within the kagome-layered RE_3BWO_9 family [49–53], such as Kramers Sm_3BWO_9 hosting an incommensurate spin order along the c axis [50]. Furthermore, we emphasize a striking similarity between the phase diagram of Nd_3BWO_9 and those of spin-ice systems, as evidenced by their shared strong Ising anisotropy and proximate ZPE state — a hallmark of spin-ice physics. In both classical (e.g., $\text{Dy}_2\text{Ti}_2\text{O}_7$ [22–25]) and quantum (e.g., $\text{Pr}_2\text{Zr}_2\text{O}_7$ [28, 29]) spin ices, there exist a first-order metamagnetic transition line terminated at a CEP, above which a supercritical regime emerges. The global shortage of helium-3 motivates the search for alternative refrigerant systems [32, 54, 55]. Our findings highlight the significant application potential of compounds such as Nd_3BWO_9 and spin-ices as promising supercritical refrigerants for extreme cooling.

Acknowledgments.— E.L. and W.L. are grateful to Yuan Gao, Junsen Wang, Yang Qi, and Frederic Mila for insightful discussions. K.Z. extends thanks to Xingye Lu for valuable experimental assistance. This work was supported by the National Key Projects for Research and Development of China (Grant Nos. 2024YFA1409200 and 2023YFA1406003), the National Natural Science Foundation of China (Grant Nos. 12534009, 12447101, 12404180, and 12274015), the Strategic Priority Research Program of Chinese Academy of Sciences (Grant No. XDB1270100), the Beijing Natural Science Foundation (Grant No. JQ24012), and the Fundamental Research Funds for the Central Uni-

versities. We thank the HPC-ITP for the technical support and generous allocation of CPU time. We acknowledge the support from the Synergetic Extreme Condition User Facility (SECUF, <https://cstr.cn/31123.02.SECUF>) and the facilities and technical support of the Extreme Condition Characterization Platform at Analysis & Testing Center of Beihang University.

* These authors contributed equally to this work.

† kan_zhao@buaa.edu.cn

‡ xiangjis@iphy.ac.cn

§ w.li@itp.ac.cn

- [1] S. Sachdev, Quantum magnetism and criticality, *Nature Physics* **4**, 173 (2008).
- [2] S. Sachdev, Quantum criticality: Competing ground states in low dimensions, *Science* **288**, 475 (2000).
- [3] L. Balents, Spin liquids in frustrated magnets, *Nature* **464**, 199 (2010).
- [4] S. Sachdev, *Quantum phase transitions*, 2nd ed. (Cambridge University Press, Cambridge, 2015).
- [5] Y. Zhou, K. Kanoda, and T.-K. Ng, Quantum spin liquid states, *Rev. Mod. Phys.* **89**, 025003 (2017).
- [6] C. Broholm, R. J. Cava, S. A. Kivelson, D. G. Nocera, M. R. Norman, and T. Senthil, Quantum spin liquids, *Science* **367**, eaay0668 (2020).
- [7] L. S. Wu, S. E. Nikitin, Z. Wang, W. Zhu, C. D. Batista, A. M. Tsvelik, A. M. Samarakoon, D. A. Tennant, M. Brando, L. Vaychlechko, M. Frontzek, A. T. Savici, G. Sala, G. Ehlers, A. D. Christianson, M. D. Lumsden, and A. Podlesnyak, Tomonaga-Luttinger liquid behavior and spinon confinement in YbAlO_3 , *Nature Communications* **10**, 698 (2019).
- [8] L. L. Kish, A. Weichselbaum, D. M. Pajerowski, A. T. Savici, A. Podlesnyak, L. Vaychlechko, A. Tsvelik, R. Konik, and I. A. Zaliznyak, High-temperature quantum coherence of spinons in a rare-earth spin chain, *Nature Communications* **16**, 6594 (2025).
- [9] Y. Shen, Y.-D. Li, H. Wo, Y. Li, S. Shen, B. Pan, Q. Wang, H. C. Walker, P. Steffens, M. Boehm, Y. Hao, D. L. Quintero-Castro, L. W. Harriger, M. D. Frontzek, L. Hao, S. Meng, Q. Zhang, G. Chen, and J. Zhao, Evidence for a spinon fermi surface in a triangular-lattice quantum-spin-liquid candidate, *Nature* **540**, 559 (2016).
- [10] H. Li, Y. D. Liao, B.-B. Chen, X.-T. Zeng, X.-L. Sheng, Y. Qi, Z. Y. Meng, and W. Li, Kosterlitz-Thouless melting of magnetic order in the triangular quantum Ising material TmMgGaO_4 , *Nature Communications* **11**, 1111 (2020).
- [11] Z. Hu, Z. Ma, Y.-D. Liao, H. Li, C. Ma, Y. Cui, Y. Shangguan, Z. Huang, Y. Qi, W. Li, Z. Y. Meng, J. Wen, and W. Yu, Evidence of the Berezinskii-Kosterlitz-Thouless phase in a frustrated magnet, *Nature Communications* **11**, 5631 (2020).
- [12] A. Brassington, Q. Huang, A. A. Aczel, and H. D. Zhou, Synthesis and magnetic properties of the shastry-sutherland family $R_2\text{Be}_2\text{SiO}_7$ ($R = \text{Nd, Sm, Gd-Yb}$), *Phys. Rev. Mater.* **8**, 014005 (2024).
- [13] A. Liu, J. Zhou, L. Wang, Y. Cao, F. Song, Y. Han, J. Li, W. Tong, Z. Xia, Z. Ouyang, J. Zhao, H. Guo, and Z. Tian, Large magnetocaloric effect in the shastry-sutherland lattice compound $\text{Yb}_2\text{Be}_2\text{GeO}_7$ with spin-disordered ground state, *Phys. Rev. B* **110**, 144445 (2024).

[14] V. A. Krut'ko, A. A. Belik, and G. V. Lysanova, Structures of nonlinear hexagonal borotungstates Ln_3BWO_9 ($\text{Ln} = \text{La, Pr, Nd, Sm, Gd, Tb, Dy}$), *Russian Journal of Inorganic Chemistry* **51**, 884 (2006).

[15] M. Ashtar, J. Guo, Z. Wan, Y. Wang, G. Gong, Y. Liu, Y. Su, and Z. Tian, A New Family of Disorder-Free Rare-Earth-Based Kagome Lattice Magnets: Structure and Magnetic Characterizations of RE_3BWO_9 ($\text{RE} = \text{Pr, Nd, Gd-Ho}$) Borotungstates, *Inorganic Chemistry* **59**, 5368 (2020).

[16] D. Flavián, J. Nagl, S. Hayashida, M. Yan, O. Zaharko, T. Fen nell, D. Khalyavin, Z. Yan, S. Gvasaliya, and A. Zheludev, Magnetic phase diagram of the breathing-kagome antiferromagnet Nd_3BWO_9 , *Phys. Rev. B* **107**, 174406 (2023).

[17] J. Nagl, D. Flavián, B. Duncan, S. Hayashida, O. Zaharko, E. Ressouche, J. Ollivier, Z. Yan, S. Gvasaliya, and A. Zhe ludev, Braided Ising spin-tube physics in a purported kagome magnet, *Phys. Rev. B* **111**, L180406 (2025).

[18] F. Song, H. Ge, A. Liu, Y. Qin, Y. Han, L. Ling, S. Yuan, Z. Ouyang, J. Sheng, L. Wu, and Z. Tian, Magnetic field tuned anisotropic quantum phase transition in the distorted kagome antiferromagnet Nd_3BWO_9 , *Phys. Rev. B* **108**, 214410 (2023).

[19] A. Yadav, A. Elghandour, T. Arh, D. T. Adroja, M. D. Le, G. B. G. Stenning, M. Aouane, S. Luther, F. Hotz, T. J. Hicken, H. Luetkens, A. Zorko, R. Klingeler, and P. Khuntia, Magnetism in the $J_{\text{eff}} = \frac{1}{2}$ kagome antiferromagnet Nd_3BWO_9 : Thermodynamics, nuclear magnetic resonance, muon spin resonance, and inelastic neutron scattering studies, *Phys. Rev. B* **111**, 094408 (2025).

[20] X. Li and Y. Jin, Thermodynamic crossovers in supercritical fluids, *Proc. Natl. Acad. Sci.* **121** (2024).

[21] C. Cyuan-Han, D. Vasiliy, E. Rajeev S., H. Alexandre, K. Petr, L. Aike, M. Matthew S., P. David, and S.-D. David, Bootstrapping the 3d Ising stress tensor, *J. High Energ. Phys.* **2025**, 136.

[22] A. P. Ramirez, A. Hayashi, R. J. Cava, R. Siddharthan, and B. S. Shastry, Zero-point entropy in 'spin ice', *Nature* **399**, 333 (1999).

[23] H. Aoki, T. Sakakibara, K. Matsuhira, and Z. Hiroi, Magnetocaloric Effect Study on the Pyrochlore Spin Ice Compound $\text{Dy}_2\text{Ti}_2\text{O}_7$ in a [111] Magnetic Field, *Journal of the Physical Society of Japan* **73**, 2851 (2004).

[24] D. J. P. Morris, D. A. Tennant, S. A. Grigera, B. Klemke, C. Castelnovo, R. Moessner, C. Czternasty, M. Meissner, K. C. Rule, J.-U. Hoffmann, K. Kiefer, S. Gerischer, D. Slobinsky, and R. S. Perry, Dirac Strings and Magnetic Monopoles in the Spin Ice $\text{Dy}_2\text{Ti}_2\text{O}_7$, *Science* **326**, 411 (2009).

[25] D. Pomaranski, L. R. Yaraskavitch, S. Meng, K. A. Ross, H. M. L. Noad, H. A. Dabkowska, B. D. Gaulin, and J. B. Ky cia, Absence of Pauling's residual entropy in thermally equilibrated $\text{Dy}_2\text{Ti}_2\text{O}_7$, *Nature Physics* **9**, 353 (2013).

[26] S. T. Bramwell and M. J. P. Gingras, Spin Ice State in Frustrated Magnetic Pyrochlore Materials, *Science* **294**, 1495 (2001).

[27] C. Castelnovo, R. Moessner, and S. L. Sondhi, Magnetic monopoles in spin ice, *Nature* **451**, 42 (2008).

[28] N. Tang, Y. Gritsenko, K. Kimura, S. Bhattacharjee, A. Sakai, M. Fu, H. Takeda, H. Man, K. Sugawara, Y. Matsumoto, Y. Shimura, J. Wen, C. Broholm, H. Sawa, M. Takigawa, T. Sakakibara, S. Zherlitsyn, J. Wosnitza, R. Moessner, and S. Nakatsuji, Spin-orbital liquid state and liquid-gas metamagnetic transition on a pyrochlore lattice, *Nature Physics* **19**, 92 (2023).

[29] J.-J. Wen, S. M. Koohpayeh, K. A. Ross, B. A. Trump, T. M. McQueen, K. Kimura, S. Nakatsuji, Y. Qiu, D. M. Pajerowski, J. R. D. Copley, and C. L. Broholm, Disordered Route to the Coulomb Quantum Spin Liquid: Random Transverse Fields on Spin Ice in $\text{Pr}_2\text{Zr}_2\text{O}_7$, *Phys. Rev. Lett.* **118**, 107206 (2017).

[30] J. D. Thompson, P. A. McClarty, D. Prabhakaran, I. Cabrera, T. Guidi, and R. Coldea, Quasiparticle Breakdown and Spin Hamiltonian of the Frustrated Quantum Pyrochlore $\text{Yb}_2\text{Ti}_2\text{O}_7$ in a Magnetic Field, *Phys. Rev. Lett.* **119**, 057203 (2017).

[31] J. Gaudet, E. M. Smith, J. Dudemaine, J. Beare, C. R. C. Buhariwalla, N. P. Butch, M. B. Stone, A. I. Kolesnikov, G. Xu, D. R. Yahne, K. A. Ross, C. A. Marjerrison, J. D. Garrett, G. M. Luke, A. D. Bianchi, and B. D. Gaulin, Quantum Spin Ice Dynamics in the Dipole-Octupole Pyrochlore Magnet $\text{Ce}_2\text{Zr}_2\text{O}_7$, *Phys. Rev. Lett.* **122**, 187201 (2019).

[32] J. Xiang, C. Zhang, Y. Gao, W. Schmidt, K. Schmalzl, C.-W. Wang, B. Li, N. Xi, X.-Y. Liu, H. Jin, G. Li, J. Shen, Z. Chen, Y. Qi, Y. Wan, W. Jin, W. Li, P. Sun, and G. Su, Giant magnetocaloric effect in spin supersolid candidate $\text{Na}_2\text{BaCo}(\text{PO}_4)_2$, *Nature* **625**, 270 (2024).

[33] H. Xie, L. Tian, Q. Chen, H. Sun, X. Gao, Z. Li, Z. Mo, and J. Shen, Giant and reversible low field magnetocaloric effect in LiHoF_4 compound, *Dalton Trans.* **50**, 17697 (2021).

[34] A. Wendl, H. Eisenlohr, F. Rucker, C. Duvinage, M. Kleinhans, M. Vojta, and C. Pfleiderer, Emergence of mesoscale quantum phase transitions in a ferromagnet, *Nature* **609**, 65 (2022).

[35] P. Liu, D. Yuan, C. Dong, G. Lin, E. G. Víllora, J. Qi, X. Zhao, K. Shimamura, J. Ma, J. Wang, Z. Zhang, and B. Li, Ultralow-field magnetocaloric materials for compact magnetic refrigeration, *NPG Asia Materials* **15**, 41 (2023).

[36] J. W. Ackerman, Pseudoboiling Heat Transfer to Supercritical Pressure Water in Smooth and Ribbed Tubes, *Journal of Heat Transfer* **92**, 490 (1970).

[37] A. A. Clifford and J. R. Williams, Introduction to Supercritical Fluids and Their Applications, in *Supercritical Fluid Methods and Protocols*, edited by J. R. Williams and A. A. Clifford (Human Press, Totowa, NJ, 2000) pp. 1–16.

[38] H. Samuel, U. Nweke-Maraizu, and E. E. Etim, Supercritical fluids: Properties, formation and applications, *Journal of Engineering in Industrial Research* **4**, 176 (2023).

[39] M.-H. Kim, J. Pettersen, and C. W. Bullard, Fundamental process and system design issues in CO_2 vapor compression systems, *Progress in Energy and Combustion Science* **30**, 119 (2004).

[40] J. L. Jiménez, S. P. G. Crone, E. Fogh, M. E. Zayed, R. Lortz, E. Pomjakushina, K. Conder, A. M. Läuchli, L. Weber, S. Wessel, A. Honecker, B. Normand, C. Rüegg, P. Corboz, H. M. Rønnow, and F. Mila, A quantum magnetic analogue to the critical point of water, *Nature* **592**, 370 (2021).

[41] J. Wang, H. Li, N. Xi, Y. Gao, Q.-B. Yan, W. Li, and G. Su, Plaquette singlet transition, magnetic barocaloric effect, and spin supersolidity in the Shastry-Sutherland model, *Phys. Rev. Lett.* **131**, 116702 (2023).

[42] J. Wang, E. Lv, X. Li, Y. Jin, and W. Li, Quantum supercritical crossover with dynamical singularity, *Phys. Rev. B* **112**, 195120 (2025).

[43] E. Lv, N. Xi, Y. Jin, and W. Li, Quantum supercritical regime with universal magnetocaloric scaling in Ising magnets, *Nature Communications* **16**, 10646 (2025).

[44] Z. Wu, T. I. Weinberger, A. J. Hickey, D. V. Chichinadze, D. Shaffer, A. Cabala, H. Chen, M. Long, T. J. Brumm, W. Xie, Y. Ling, Z. Zhu, Y. Skourski, D. E. Graf, V. Sechovský, M. Vališka, G. G. Lonzarich, F. M. Grosche, and A. G. Eaton, A Quantum Critical Line Bounds the High Field Metamagnetic Transition Surface in UTe_2 , *Phys. Rev. X* **15**, 021019 (2025).

[45] S. K. Lewin, P. Czajka, C. E. Frank, G. S. Salas, G. T. N. II, H. Yoon, Y. S. Eo, J. Paglione, A. H. Nevidomskyy, J. Singleton, and N. P. Butch, High-field superconducting halo in UTe_2 ,

Science **389**, 512 (2025).

[46] P. Weiss and A. Piccard, Le phénomène magnétocalorique, *J. Phys. (Paris)* **7**, 103 (1917).

[47] Y. Wang, J. Xiang, L. Zhang, J. Gong, W. Li, Z. Mo, and J. Shen, Giant low-field cryogenic magnetocaloric effect in a polycrystalline EuB_4O_7 compound, *Journal of the American Chemical Society* **146**, 3315 (2024).

[48] Z. Mo, J. Jiang, L. Tian, H. Xie, Y. Li, X. Zheng, L. Zhang, X. Gao, Z. Li, G. Liu, L. Li, and J. Shen, Ferromagnetic Eu_2SiO_4 Compound with a Record Low-Field Magnetocaloric Effect and Excellent Thermal Conductivity Near Liquid Helium Temperature, *Journal of the American Chemical Society* **147**, 14684 (2025).

[49] K. Y. Zeng, F. Y. Song, Z. M. Tian, Q. Chen, S. Wang, B. Liu, S. Li, L. S. Ling, W. Tong, L. Ma, and L. Pi, Local evidence for collective spin excitations in the distorted kagome antiferromagnet Pr_3BWO_9 , *Phys. Rev. B* **104**, 155150 (2021).

[50] K.-Y. Zeng, F.-Y. Song, L.-S. Ling, W. Tong, S.-L. Li, Z.-M. Tian, L. Ma, and L. Pi, Incommensurate Magnetic Order in Sm_3BWO_9 with Distorted Kagome Lattice, *Chinese Physics Letters* **39**, 107501 (2022).

[51] J. Nagl, D. Flavián, S. Hayashida, K. Y. Povarov, M. Yan, N. Murai, S. Ohira-Kawamura, G. Simutis, T. J. Hicken, H. Luetkens, C. Baines, A. Hauspurg, B. V. Schwarze, F. Husstedt, V. Pomjakushin, T. Fennell, Z. Yan, S. Gvasaliya, and A. Zheludev, Excitation spectrum and spin Hamiltonian of the frustrated quantum Ising magnet Pr_3BWO_9 , *Phys. Rev. Res.* **6**, 023267 (2024).

[52] F. Song, X. Liu, C. Dong, J. Zhou, X. Shi, Y. Han, L. Ling, H. Ren, S. Yuan, S. Wang, J. Xiang, P. Sun, and Z. Tian, Realization of Large Magnetocaloric Effect in the Kagome Antiferromagnet Gd_3BWO_9 for Sub-Kelvin Cryogenic Refrigeration, *Chin. Phys. Lett.* **42**, 120706 (2025).

[53] Z. Wang, X. Cui, T. Treu, J. Guo, X. Liu, M. Klinger, C. Heil, N. Ma, X. Sheng, Z. Deng, X. Lu, X. Wang, W. Li, P. Gegenwart, C. Jin, and K. Zhao, Antiferromagnetic ordering and critical behavior induced giant magnetocaloric effect in distorted kagome lattice Gd_3BWO_9 , *Phys. Rev. Mater.* **9**, 094407 (2025).

[54] D. Kramer, Helium users are at the mercy of suppliers, *Phys. Today* **72**, 26 (2019).

[55] A. Cho, Helium-3 shortage could put freeze on low-temperature research, *Science* **326**, 778 (2009).

[56] T. Liang, S. M. Koohpayeh, J. W. Krizan, T. M. McQueen, R. J. Cava, and N. P. Ong, Heat capacity peak at the quantum critical point of the transverse Ising magnet CoNb_2O_6 , *Nature Communications* **6**, 7611 (2015).

Appendix

Sample synthesis and characterization.— Single crystals of Nd_3BWO_9 were synthesized using the PbO flux method. A mixture of Nd_3BWO_9 powder and PbO in a 1:14 molar ratio was thoroughly ground and placed in a platinum crucible. The crucible was heated to 1150 °C, held at for 25 h, cooled to 900 °C at a rate of 2.5 °C/h, and finally cooled to room temperature at 100 °C/h. Crystals were separated by etching in a hot acidic solution, as shown in the left inset of Fig. 5(a). X-ray diffraction pattern of the bc plane display dominant (H00) reflections at room temperature, using a Bruker D8 ADVANCE diffractometer with Cu-K α radiation ($\lambda = 1.5406$ Å). Rocking curve analysis of the Bragg peak (200), right inset of Fig. 5(a), demonstrates a narrow full width at half maximum (FWHM) of 0.16°, indicating high quality of the single crystal.

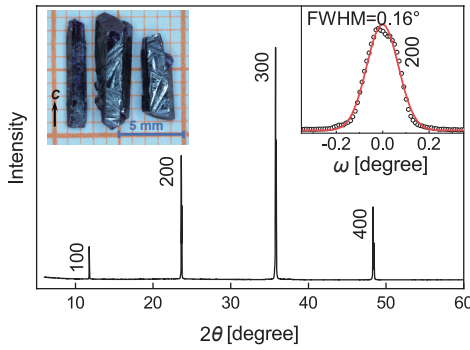


FIG. 5. X-ray diffraction pattern of Nd_3BWO_9 single crystal. Left inset: an optical image of typical single crystals. Right inset: the rocking curve (black line) of the (200) Bragg peak, together with the Gaussian fitting (red line).

Thermodynamic and magnetocaloric measurements.— Specific heat measurements above 2 K were performed using the standard heat capacity puck of the Physical Property Measurement System (PPMS). Ultralow-temperature specific heat measurements were carried out using the quasi-adiabatic heat-pulse method, and magnetization measurements down to 50 mK were performed using a Hall-sensor magnetometer, both implemented in a PPMS equipped with a ^3He - ^4He dilution refrigerator.

Quasi-adiabatic demagnetization refrigeration (ADR) data were acquired using a custom-designed setup based on the PPMS under various initial conditions. Thermal insulation is achieved by employing low thermal-conductivity support structures and a high-vacuum environment. Multiple single crystals of Nd_3BWO_9 (total mass 1.5 g) were aligned in the same direction and used as samples, and their temperature was monitored using a calibrated RuO_2 thermometer. The magnetic field was applied along the c -axis, and demagnetization was carried out at a constant sweep rate of 50 Oe/s.

Scaling analysis of universal thermodynamics.— Above a critical endpoint (CEP), the singular part of free energy pos-

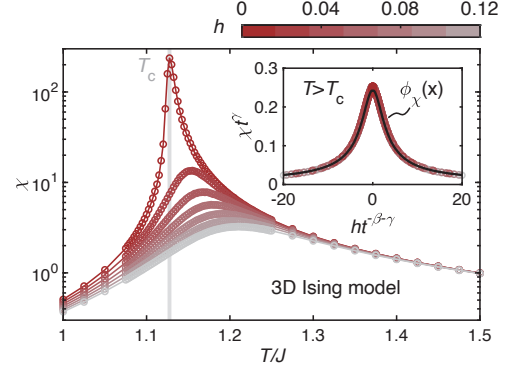


FIG. 6. The magnetic susceptibility χ of the 3D classical ferromagnetic Ising model for each fixed magnetic field h . Inset shows the supercritical data ($T > T_c$) which can be collapsed onto the 3D-Ising scaling function $\phi_\chi(x)$ (black line). The Monte Carlo calculations are conducted on a cubic lattice of $N = 40^3$ Ising spins.

sesses universal form as

$$F = t^{2-\alpha} \xi_1 \phi_F(\xi_2 h t^{-\beta-\gamma}), \text{ for } t > 0, \quad (1)$$

where $t \equiv (T - T_c)/T_c$ and $h \equiv (H - H_c)/H_c$ are reduced parameters measuring the distance to the CEP at (H_c, T_c) . β and γ are critical exponents. ξ_1 and ξ_2 are non-universal parameters and we set $\xi_1 = \xi_2 = 1$ for simplicity. Particularly, the scaling function $\phi_F(x)$ just depends on the universality class. In Nd_3BWO_9 , the emergent CEP belongs to the 3D Ising universality class. Derived from the universal form Eq. 1, thermodynamics exhibit universal behaviors near the CEP. Particularly, the specific heat can be expressed as $C \equiv -T \frac{\partial^2 F}{\partial T^2} = t^{-\alpha} \phi_C(ht^{-\beta-\gamma})$. Considering the maximum condition $\frac{\partial C}{\partial T} = 0$, the peak locations satisfy $ht^{-\beta-\gamma} = \text{const.}$, implying $h \propto t^{\beta+\gamma}$, which is illustrated in Fig. 2(c). Additionally, the magnetic susceptibility has a universal form $\chi \equiv -\frac{\partial^2 F}{\partial H^2} = t^{-\gamma} \phi_\chi(ht^{-\beta-\gamma})$. The scaling function $\phi_\chi(x)$ is obtained through data collapse, in excellent agreement with the 3D Ising scaling function calculated by Monte Carlo method, as shown in Fig. 2(e).

Below, we consider the Grüneisen ratio $\Gamma_H \equiv \frac{1}{T} \left(\frac{\partial T}{\partial H} \right)_S = -\left(\frac{\partial^2 F}{\partial H \partial T} \right) / \left(T \frac{\partial^2 F}{\partial T^2} \right)$, which characterizes the temperature variation during an adiabatic demagnetization process. Near the CEP, Grüneisen ratio also possesses a universal form

$$\Gamma_H = t^{1-\beta-\gamma} \phi_\Gamma(ht^{-\beta-\gamma}). \quad (2)$$

For an adiabatic demagnetization process, the peak/dip condition is $\left(\frac{\partial \Gamma_H}{\partial H} \right)_S = \frac{\partial \Gamma_H}{\partial H} + \left(\frac{\partial \Gamma_H}{\partial T} \right) \left(\frac{\partial T}{\partial H} \right)_S = \frac{\partial \Gamma_H}{\partial H} + \frac{\partial \Gamma_H}{\partial T} \Gamma_H T = 0$, using the definition $\Gamma_H \equiv \frac{1}{T} \left(\frac{\partial T}{\partial H} \right)_S$. Considering the universal form Eq. 2, the peak/dip condition can be expressed as $(1-\beta-\gamma) \phi_\Gamma^2(x) + \phi_\Gamma'(x) \left[\frac{1}{H_c} - (\beta+\gamma)x \phi_\Gamma(x) \right] = 0$ with $x = ht^{-\beta-\gamma}$ and the corresponding zero point is $ht^{-\beta-\gamma} = x_0$. It means that the peak/dip values measured

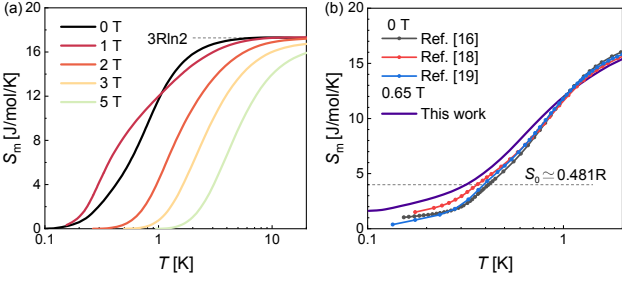


FIG. 7. (a) Magnetic entropy under different magnetic fields. (b) The measured entropy at 0 T from different groups [16, 18, 19] consistently point to a shoulder-like structure at topological domain-wall entropy $S_0 \simeq 0.481R$. The low- T entropy gets notably enhanced under 0.65 T as the domain walls proliferate at lower temperatures.

by adiabatic demagnetization process satisfy a universal scaling $\Gamma_H^{\text{peak/dip}} = t^{1-\beta-\gamma} \phi_\Gamma(x_0) \propto t^{1-\beta-\gamma}$ because $\phi_\Gamma(x_0)$ is a constant, as shown in the inset of Fig. 3(d).

Supercritical scaling function of 3D Ising universality class.— Since universal scaling functions characterize a universality class regardless of microscopic details, the scaling function $\phi_\chi(x)$ for the 3D Ising class can be obtained by studying a canonical minimal model. We thus employ Monte Carlo simulations of the classical ferromagnetic (FM) Ising model on a cubic lattice,

$$H_{\text{Ising}} = -J \sum_{\langle i,j \rangle} S_i^z S_j^z - h \sum_i S_i^z, \quad (3)$$

where $J = 1$ is the FM Ising coupling and h denotes the longitudinal field. Our calculations are performed on a cubic lattice of size $N = 40^3$. From the magnetic susceptibility χ , we identify a critical temperature $T_c \simeq 1.13$ for the finite-size system (see Fig. 6). For $h \neq 0$, the phase transition evolves into a crossover characterized by a broad peak at higher temperatures. To obtain the supercritical scaling function $\phi_\chi(x)$, we perform a collapse using the $T > T_c$ data. The calculated $\phi_\chi(x)$, shown in the inset, agrees well with the experimental data presented in Fig. 2(e) of the main text. Notably, non-universal parameters in Eq. (1) allow us to rescale the x and y axes to match the experimental results.

Entropy curves under various fields.— Fig. 7(a) shows the entropy curves $S_m(T)$ under various fields. The zero-field magnetic entropy reaches a saturation value $3R \ln 2$ at high temperature. Figure 7(b) displays the entropy values near the zero field, where a shoulder-like structure corresponding to a ZPE of $S_0 \simeq 0.481R$ can be recognized. At the spin-flip field $\mu_0 H_{\text{SF}} \simeq 0.65$ T, we find further enhanced low- T entropy, ascribed to the proliferation of topological domain-wall excitations.

Zero-point entropy of spiral Ising tube.— Here, we compute the isentropes of the spiral Ising tube (SIT) model for

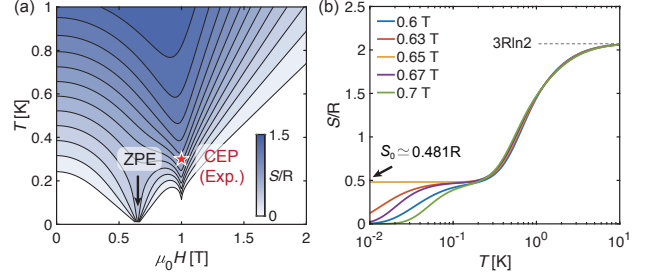


FIG. 8. (a) Isentropic lines of the effective Ising tube model. Arrow illustrates the spin-flip transition field $\mu_0 H_{\text{SF}} \simeq 0.65$ T. The saturation field $\mu_0 H_s \simeq 1$ T in Ising tube model is close to the critical field $\mu_0 H_c \simeq 1.04$ T in experiments. Red star represents the CEP observed in experiments, which is however, not present in the Ising tube model. (b) Entropy curves near the H_{SF} , where ZPE is found to be $S_0 \simeq 0.481R$.

Nd_3BWO_9 , using the transfer matrix method [17],

$$H_{\text{SIT}} = \sum_{i,j} (J_r S_{i,j}^z S_{i+1,j}^z + J_b S_{i,j}^z S_{i+1,(j-1)\text{mod}3}^z) - g_{zz} \mu_0 \mu_B \mathbf{H} \cdot \mathbf{z} \sum_{i,j} S_{i,j}^z, \quad (4)$$

where i labels the layer along the c -axis and $j = \{1, 2, 3\}$ labels three spins in a triangle in a - b plane. As shown in Fig. 1(c), the red and blue bonds represent two different Ising couplings, namely, $J_r \simeq -0.084$ meV and $J_b \simeq 0.24$ meV, respectively [17]. The angle between the magnetic field and Ising z -axis is 54° and we set the $g_{zz} \simeq 7.06$. The simulated isentropes are shown in Fig. 8(a), from which we find two prominent dips, one at the saturation field $\mu_0 H_s \simeq 1$ T and the other at the spin-flip field $\mu_0 H_{\text{SF}} \simeq 0.65$ T. Although the tube model accounts for the low-temperature cooling via ZPE [$S_0 \simeq 0.481$ R, Fig. 8(b)] near H_{SF} , the 1D model cannot capture the singular behaviors near the CEP ($\mu_0 H_c \simeq 1.04$ T, $T_c \simeq 0.3$ K) observed in experiments. These supercritical scaling behaviors are inherently 3D, arising from both intra- and inter-tube couplings (see Supplementary Fig. S2).

In the spiral AF phase, there exists a three-rung period along the spin tube, with the ground-state energy persist $\varepsilon_{\text{AF}} = S^2(-J_b - |J_r|/3)$ ($S = 1/2$ is the effective Ising spin). The three spins within the same layer [i.e., on the a - b plane in Fig. 1(c)] can be collectively described by a single effective spin, which represents either the (up-up-down) UUD or (down-down-up) DDU configuration (see Supplementary Fig. S3). The effective spins form an AF chain. At the spin-flip field $H_{\text{SF}} = 2S(J_b - |J_r|)$, domain walls, as topological defects, emerge and can move freely without energy cost, i.e., $\varepsilon_{\text{DW}} = 2S^2(J_b - |J_r|) - H_{\text{SF}}S = 0$. For an N -site effective spin chain, the degeneracy is $\Omega = \sum_{i=N/2}^N \frac{(i+1)!}{(N-i)!(2i-N+1)!}$. Consequently, the ZPE per unit cell at H_{SF} reads $S_0 = \lim_{N \rightarrow \infty} \frac{1}{N} \ln \Omega \simeq 0.481$. For $H \gtrsim H_{\text{SF}}$, there exists a domain wall on every bond, and the system is in the spiral plateau phase (all UUD) of the original Ising tube.

Supplementary Materials for

Ising Supercriticality and Universal Magnetocalorics in Spiral Ising Antiferromagnet Nd_3BWO_9 *Liu et al.*

Materials	Class	Effective spin	T_c (K)	N (nm $^{-3}$)	S_m^V (mJ·K $^{-1}·\text{cm}^{-3}$)	S_m^V/T_c (mJ·K $^{-2}·\text{cm}^{-3}$)	Ref.
Nd₃BWO₉	Spiral AF	1/2	0.3	16.9	161.6	538.7	This work
Dy ₂ Ti ₂ O ₇	Spin Ice	1/2	0.36	15.4	147.8	410.5	[23]
Pr ₂ Zr ₂ O ₇	Spin Ice	1/2	0.06	13.0	124.6	2077	[28]
LiHoF ₄	FM	1/2	1.53	13.7	131.1	85.69	[35]
LiTbF ₄	FM	1/2	2.87	13.5	129.6	45.16	[35]
CoNb ₂ O ₆	FM	1/2	2.85	9.86	94.37	33.11	[56]
Eu ₂ SiO ₄	FM	7/2	4.2	20.5	587.7	139.9	[48]

TABLE I. Comparison of spiral Ising antiferromagnet (AF) Nd₃BWO₉ to spin-ice magnets and typical ferromagnetic (FM) refrigerants, including the effective spin, critical temperature T_c , magnetic ion density N , and volumetric magnetic entropy S_m^V .

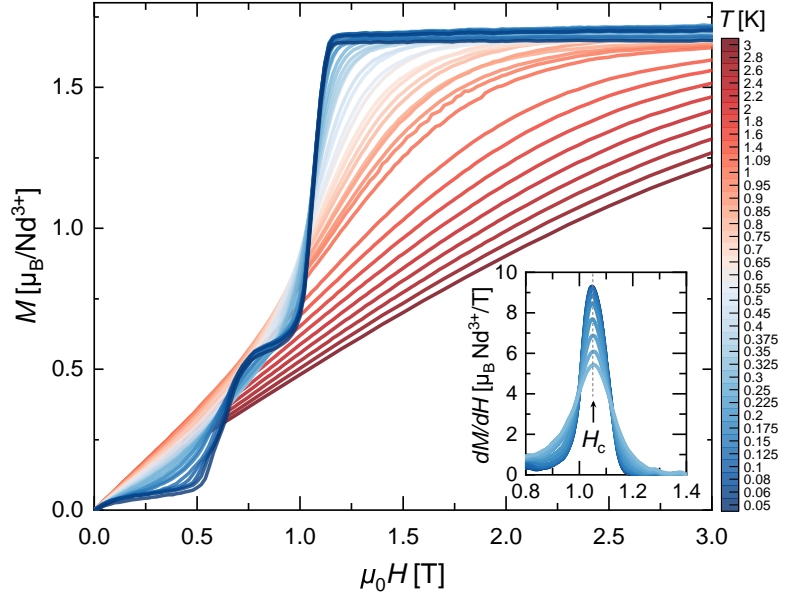


FIG. S1. The isothermal field-dependent magnetization $M(H)$ curves of Nd_3BWO_9 single crystal measured down to 50 mK for field $H \parallel c$. Inset shows the magnetic susceptibility $\chi \equiv dM/dH$ vs. H at various temperatures, with the peak marking the first-order metamagnetic transition $\mu_0 H_c \simeq 1.04$ T.

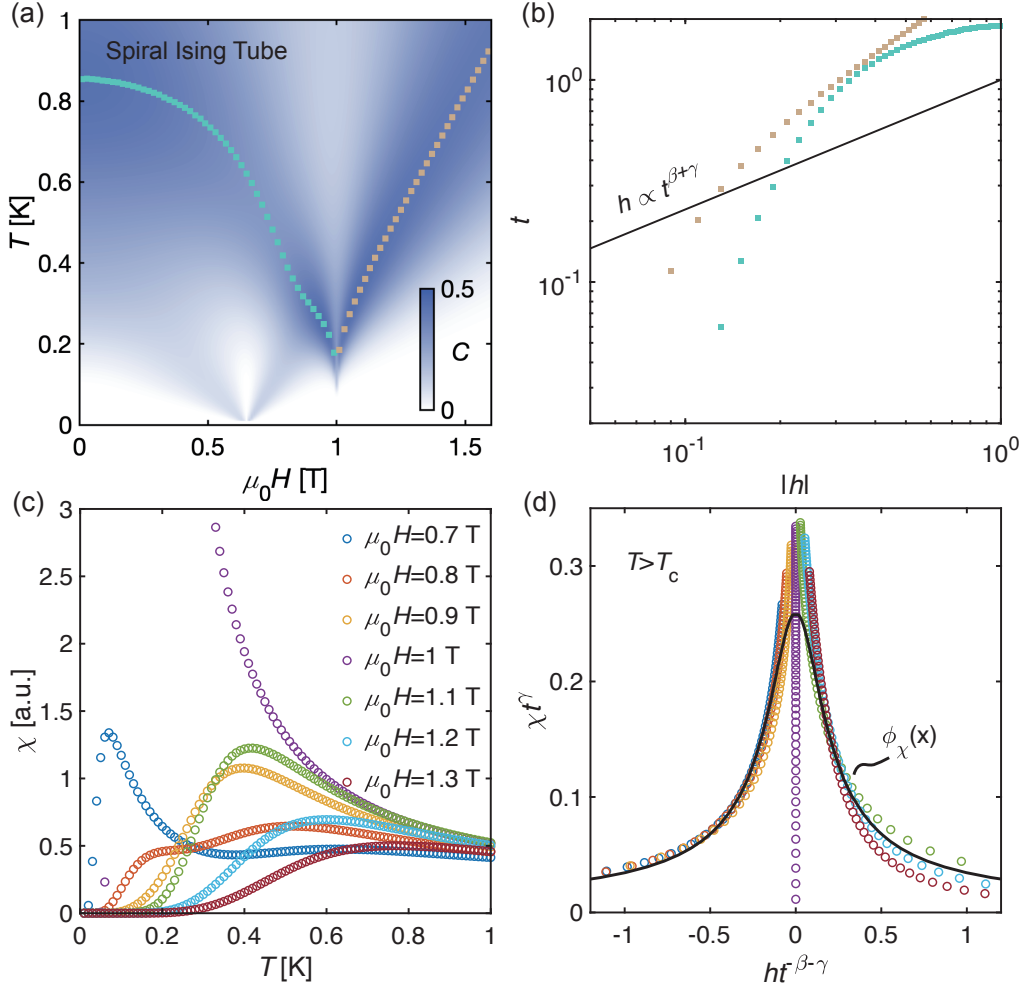


FIG. S2. Results of the spiral Ising tube model versus 3D Ising universal behaviors. (a) The specific heat results. Squares represent the peak positions for each fixed magnetic field. (b) The peak positions of C do not follow the $h \propto t^{\beta+\gamma}$ scaling (black line) of supercritical crossovers, with $h = (H - H_c)/H_c$ and $t = (T - T_c)/T_c$ the reduced parameters. (c) The magnetic susceptibility results near the saturation field $\mu_0 H_s \simeq 1$ T. (d) Data collapse of the susceptibility χ in (c). Black line indicates the universal scaling function $\phi_\chi(x)$ of the 3D Ising universality class shown in the Fig. 2(f) of the main text. As shown above, the spiral Ising tube model can not describe the Ising supercriticality in the main text.

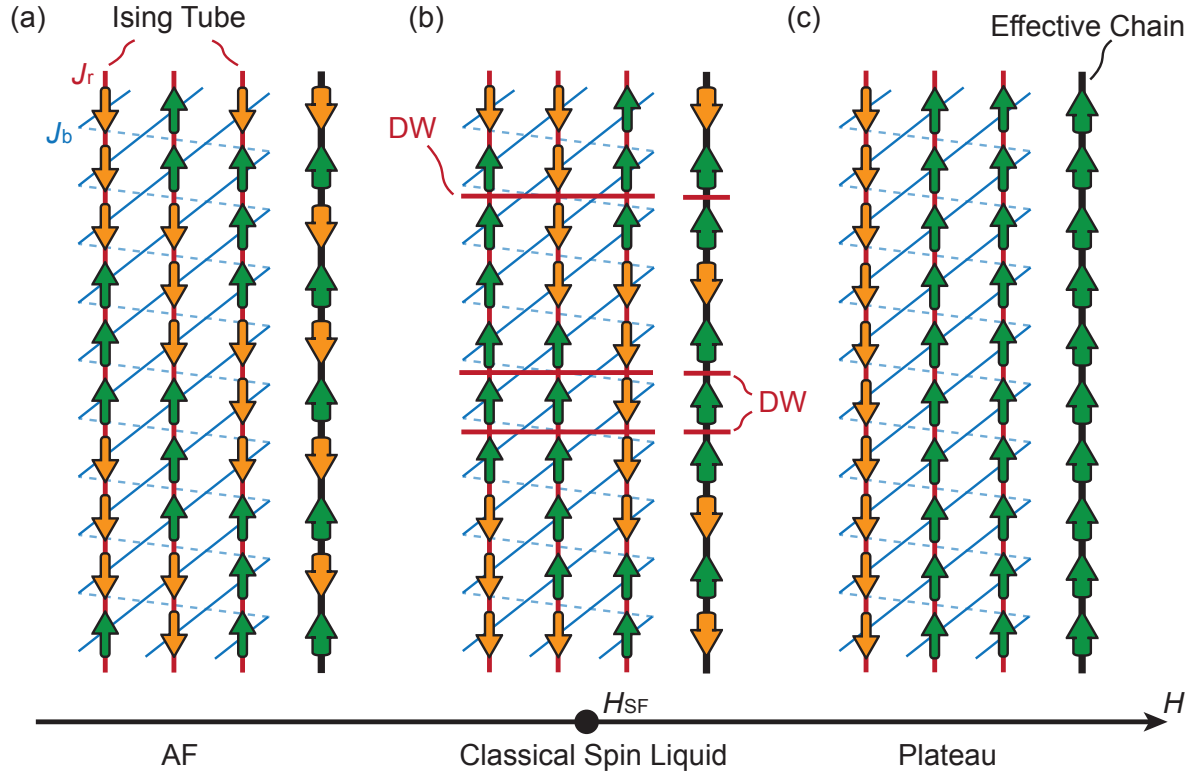


FIG. S3. Domain wall (DW) excitation in the classical spin liquid at H_{SF} . To simplify, we only illustrate the projection along the FM ladder, since the spin is constrained to follow the Ising axis. The red leg represents the FM coupling $J_r < 0$ and the blue rung is the AF coupling $J_b > 0$. The thick spins form an effective representation of the spin tube.